

KIF14 Binds Tightly to Microtubules and Adopts a Rigor-Like Conformation

Kritica Arora^{1,†}, Lama Talje^{2,†}, Ana B. Asenjo³, Parker Andersen², Kaleem Atchia², Monika Joshi¹, Hernando Sosa³, John S. Allingham¹ and Benjamin H. Kwok²

1 - Department of Biomedical and Molecular Sciences, Queen's University, 18 Stuart St., Rm. 652, Kingston, ON K7L 3 N6, Canada

2 - Institute for Research in Immunology and Cancer, Département de Médecine, Université de Montréal, P.O. Box 6128, Station Centre-Ville, Montréal, QC H3C 3 J7, Canada

3 - Department of Physiology and Biophysics, Albert Einstein College of Medicine, Bronx, NY 10461, USA

Correspondence to John S. Allingham and Benjamin H.

Kwok: allinghj@queensu.ca; benjamin.kwok@umontreal.ca

<http://dx.doi.org/10.1016/j.jmb.2014.05.030>

Edited by J. Sellers



Kritica Arora, Lama Talje, John S. Allingham and Benjamin H. Kwok

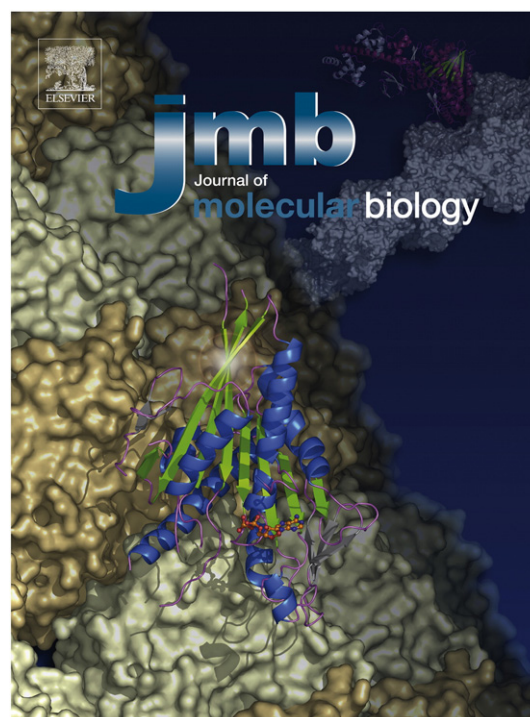
Abstract

The mitotic kinesin motor protein KIF14 is essential for cytokinesis during cell division and has been implicated in cerebral development and a variety of human cancers. Here we show that the mouse KIF14 motor domain binds tightly to microtubules and does not display typical nucleotide-dependent changes in this affinity. It also has robust ATPase activity but very slow motility. A crystal structure of the ADP-bound form of the KIF14 motor domain reveals a dramatically opened ATP-binding pocket, as if ready to exchange its bound ADP for Mg·ATP. In this state, the central β -sheet is twisted $\sim 10^\circ$ beyond the maximal amount observed in other kinesins. This configuration has only been seen in the nucleotide-free states of myosins—known as the “rigor-like” state. Fitting of this atomic model to electron density maps from cryo-electron microscopy indicates a distinct binding configuration of the motor domain to microtubules. We postulate that these properties of KIF14 are well suited for stabilizing midbody microtubules during cytokinesis.

© 2014 The Authors. Published by Elsevier Ltd. This is an open access article under the CC BY license (<http://creativecommons.org/licenses/by/3.0/>).

Introduction

The mitotic kinesin KIF14 has essential roles during cell division and has been implicated in normal development and in cancer [1–5]. Knockdown studies



Legend: Biochemical and structural characterization of the kinesin-3 motor KIF14 reveal an atypical tight binding to microtubules and a novel kinesin conformation with hyper-twisted central β -sheet (in green). This configuration, known as the rigor-like state, has only been previously observed in myosin (colored in magenta binding to F-actin and shown in the background).

0022-2836/© 2014 The Authors. Published by Elsevier Ltd. This is an open access article under the CC BY license (<http://creativecommons.org/licenses/by/3.0/>). *J. Mol. Biol.* (2014) **426**, 2997–3015

have revealed KIF14's role in the late stages of cytokinesis, with depletion of KIF14 that leads to the formation of binucleated cells resulting from failure in cytokinesis [6–8]. Homozygous mutation of human KIF14 has been shown to result in lethality [5]. On the other hand, KIF14 overexpression has been associated with multiple cancers and correlates with poor prognosis in cancer patients [4,9,10]. For this reason, KIF14 has been referred to as an oncogenic kinesin [1,3,11]. Despite its importance, our knowledge of KIF14 as a mitotic motor protein is rather limited.

During cell division, KIF14 localizes to the mitotic spindle in metaphase, to the spindle midzone in anaphase, and to the midbody during cytokinesis [7,8]. Since KIF14 depletion has resulted in cytokinesis failure, its midbody localization has drawn the most attention. Within the midbody, KIF14 has been shown to be associated with the centralspindlin complex via interaction with PRC1 and citron kinase [8]. However, the precise functions of KIF14 in the complex remain unclear. Similar to the mitotic spindle, the midbody is also composed of parallel and antiparallel microtubule bundles [12]. One major difference between them is that midbody microtubules are in general more stable than the bulk of the spindle microtubules [13,14]. In the spindle, the kinesin-5 motor Eg5 crosslinks adjacent microtubules by bundling parallel microtubules together and sliding antiparallel ones apart [15,16]. KIF14 may function in a similar manner to bind, bundle, and stabilize midbody microtubules. However, none of these aspects have been formally characterized.

KIF14 belongs to the kinesin-3 family of microtubule motors. This family also includes the well-characterized KIF1A kinesin, which functions as an anterograde motor protein that transports membranous organelles along axonal microtubules [17]. KIF1A can exist as monomers or homodimers, either of which can move processively along microtubules by coupling of ATPase activity in its N-terminally positioned motor domain to directed movement [18–22]. Crystal structures and cryo-electron microscopy (EM) images of this domain with its nucleotide-binding pocket occupied by ATP analogs or ADP have shown areas of the motor domain that are sensitive to the nucleotide- and tubulin-binding state [23–25]. This has helped generate a detailed map of the communication links between the nucleotide pocket, the microtubule, and the force producing neck linker, which compose the major elements for mechanochemical coupling in kinesins [23–25]. Very recent computational studies involving single motor domains of KIF1A have also shown that the β -sheet core undergoes a twist during phosphate release and ATP binding in molecular dynamics simulations [26], similar to myosin [27,28]. Together, with kinetic measurements of KIF1A homologs [29] and EPR spectroscopy and Förster resonance energy transfer (FRET) analysis of other N-terminal kinesin motors

[21,30,31], interpretation of KIF1A's physiological roles and its performance following mutation [32] or inhibition with small molecules is increasingly plausible. Absent, however, is a comparable understanding of KIF14.

Here we examine the biochemical and structural properties of the KIF14 motor domain (KIF14MD) and assess its interaction with microtubules. We found that KIF14 as a motor exhibited a number of unusual properties that include very high affinity for microtubules and an ability to stabilize them against low-temperature-stimulated depolymerization. According to cryo-EM studies, its motor domain assumes a slightly skewed orientation on microtubules in the presence of AMPPNP (mimicking an ATP state) compared to other kinesins. Intriguingly, the crystal structure of the KIF14 motor domain shows a wide-open nucleotide pocket and a distorted central β -sheet that is similar to the state captured for the nucleotide-free forms of myosin V and myosin II [27,28]. By analogy to actin-induced P_i and ADP release by myosin, this state has been predicted to occur during ADP release and rigor binding of the kinesin motor domain to the microtubule [33] but has not been observed in kinesin crystal structures or by cryo-EM until now. KIF14's inclination to crystallize in this “rigor-like” state could explain another of our observations; which is that the affinity of this motor for microtubules is largely insensitive to the nucleotide state of its active site.

Results

Mouse KIF14 is 1674 amino acids long and its motor domain resides between E390 and N743 (Fig. 1a). There is a high degree of primary structure homology with the motor domains of other kinesin-3 family members, such as KIF1A, but sequence conservation breaks down significantly at areas that form loops L8a, L10, L11, and L12 (also identified as the K-loop in the kinesin-3 family) [23], as well as β 7 (Fig. 1b). In addition, KIF14 has a conserved insertion in loop L8a, which is part of the microtubule-binding region. The region prior to the motor domain, toward the N-terminus, is much longer than other kinesins (residues 1–389) and appears to possess a globular structure (Fig. 1a). To understand the relationship between these divergent elements of KIF14 and its motor activity, we first purified several recombinant KIF14 motor constructs. These include mouse KIF14_N391-D772 [denoted as KIF14MD-D772: glutathione S-transferase (GST) -tagged and untagged], mouse KIF14_N391-L735 (denoted as KIF14MD-L735), and a maltose-binding protein (MBP) fusion of mouse KIF14_E390-N738 (denoted as MBP-KIF14MD-N738). We chose to focus on the mouse constructs over the human ones because of the relative ease to produce them in larger quantity and higher purity

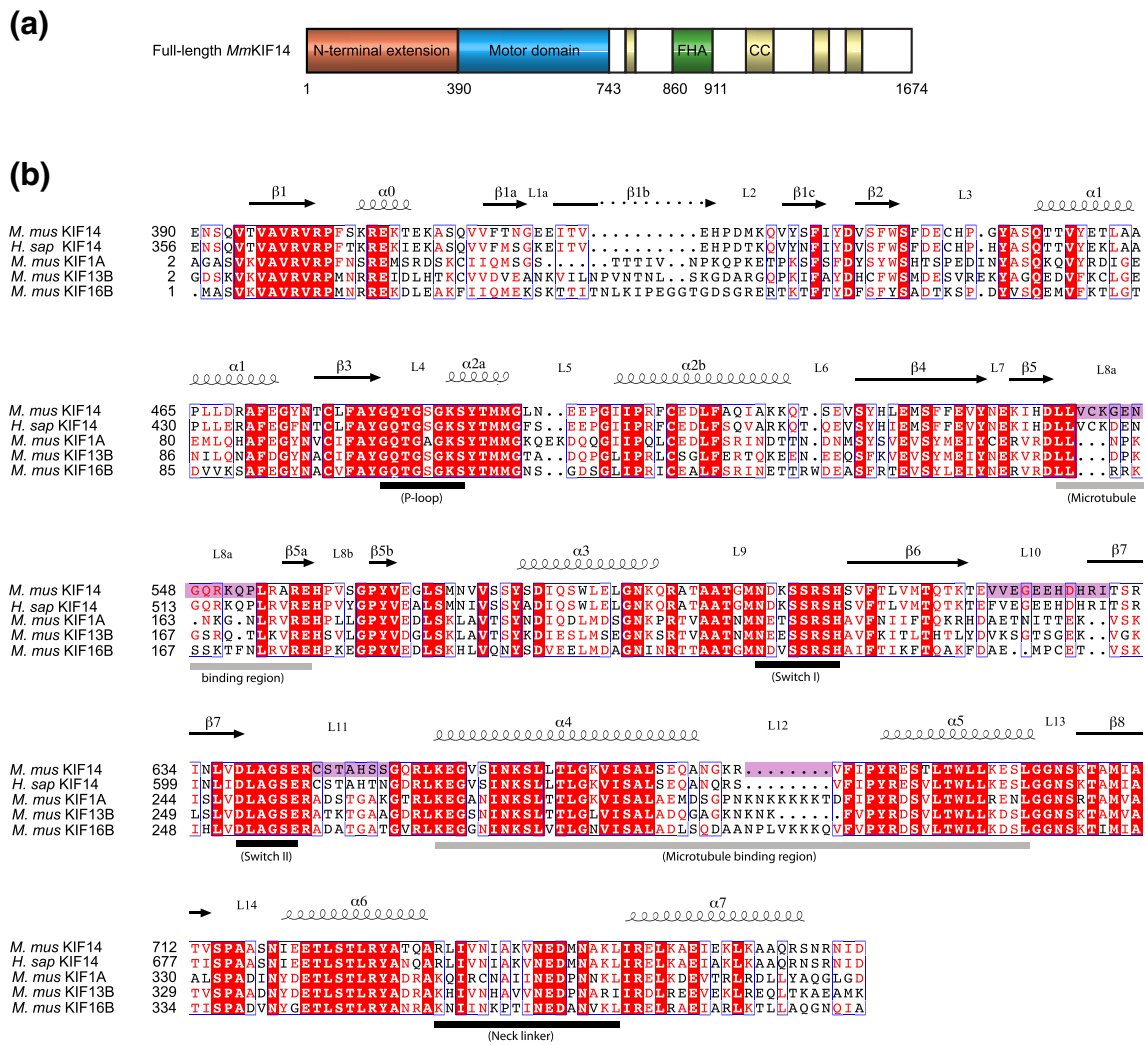


Fig. 1. Primary structure of *Mus musculus* KIF14 and sequence alignment of the motor domain of kinesin-3 family motors. (a) Regions forming the N-terminal extension, the motor domain, coiled coils (CC), and the forkhead-associated domain (FHA) are shown. (b) Both the sequence alignment and the assignment of the secondary structure for the motor domain were performed using ESPript [92] according to the MBP-KIF14MD-N738 crystal structure (PDB ID: 4OZQ). The nucleotide-binding pocket and microtubule-binding regions are shown. Significant breakdown in sequence conservation between KIF14 and other kinesin-3 motor proteins, which include loops L8a, L10, L11, and L12, as well as β7, is indicated in purple.

(Fig. S1). All KIF14MD constructs have robust and comparable ATP turnover rates (Figs. S1 and S2).

KIF14 has a robust ATPase activity

To characterize KIF14MD's enzymatic activity, we analyzed the GST-KIF14MD-D772 construct, which contains both the motor and the neck linker. We first measured its basal ATPase activity, tubulin dimer-stimulated ATPase activity, and microtubule-stimulated ATPase activity using a malachite green-based assay to detect phosphate release over time. We calibrated this detection method to ensure that the signal increase by absorbance at 620 nm followed a linear relation of phosphate increase within

the range we were measuring (Fig. S1a). Using this method, we found that GST-KIF14MD-D772 has an unusually high basal ATPase rate (at 0.88 s⁻¹; Fig. 2a) compared to other kinesins (kinesin-1: ~0.01 s⁻¹ [34,35]; kinesin-5: 0.02 s⁻¹ [36]) but similar to KIF1A (~0.5 s⁻¹ [25]). Like other kinesins, GST-KIF14MD-D772 ATPase activity can be stimulated by the presence of microtubules. Addition of microtubules increased the ATPase rate by approximately 3-fold and saturated at ~0.3 μM tubulin (Fig. 2b). This is distinct from kinesin-1 whose rate increases by ~5000-fold to 50 s⁻¹ upon microtubule stimulation [34,37]. From the microtubule titration curve, we determined the *k*_{cat} to be ~2.65 s⁻¹ and the *K*_{1/2, MT} to be about 0.02 μM. To calculate the

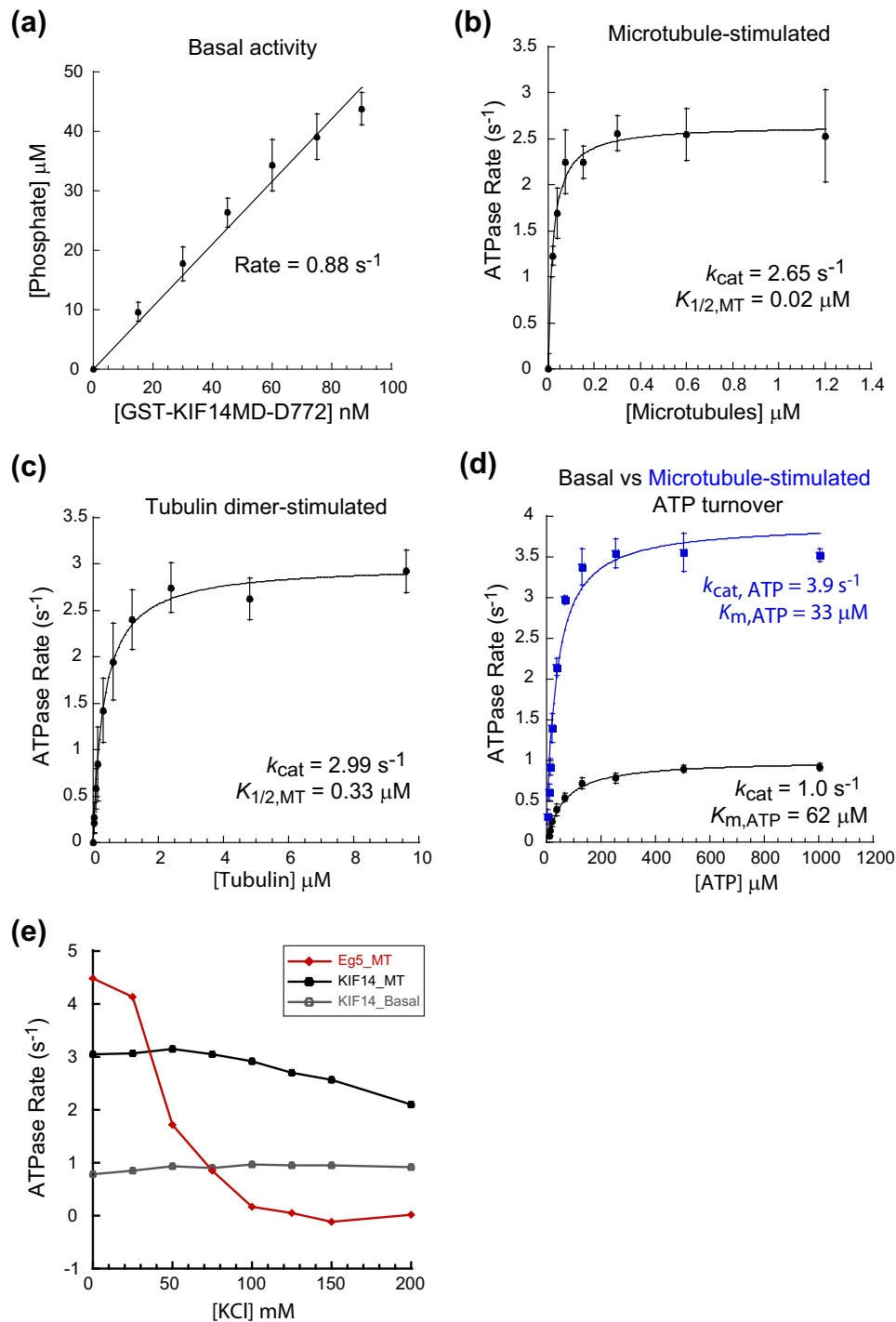


Fig. 2. ATPase activity of KIF14 motor domain. (a) Basal activity of GST-KIF14MD-D772. A plot of phosphate release in 10 min against GST-KIF14MD-D772 concentrations is shown. (b) Microtubule-stimulated ATPase activity. ATP turnover rates were plotted against microtubule concentration (calculated based on tubulin dimer concentration). $K_{1/2, \text{MT}}$ and k_{cat} values are determined by a parabolic fit to the Michaelis–Menten equation using KaleidaGraph. (c) Tubulin dimer-stimulated ATPase activity. ATPase rates were plotted against tubulin dimer concentrations. (d) An ATP concentration titration of GST-KIF14MD-D772's basal turnover rate and the microtubule-stimulated rate (blue). (e) ATP turnover rates of GST-Eg3MD and GST-KIF14MD-D772 were plotted against KCl concentrations used in the ATPase reactions. For all ATPase experiments, data points were collected as duplicates or triplicates and are shown as averages from at least three independent sets. Error bars represent standard deviations.

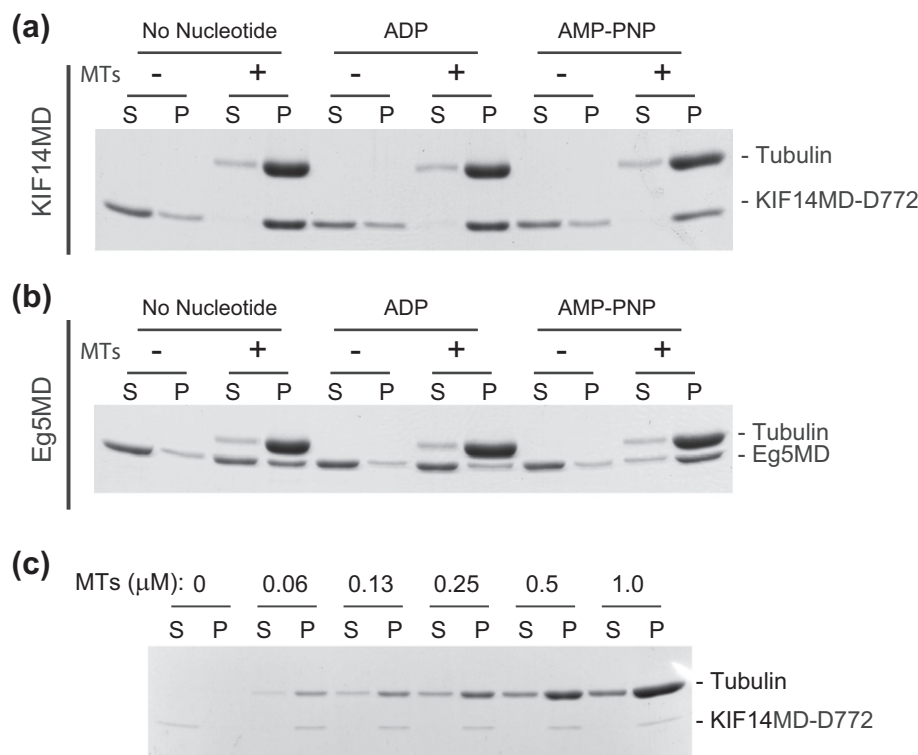


Fig. 3. KIF14 motor domain binds to microtubules with high affinity. (a and b) Microtubule co-sedimentation assay with KIF14MD-D772 (a) and Eg5MD (b) without nucleotide or in the presence of 1 mM ADP or AMPPNP, a non-hydrolyzable ATP analog. Supernatant (S) and pellet (P) fractions were resolved by SDS-PAGE and gels were stained with Coomassie blue dye. (c) A microtubule titration from 62.5 nM to 1 μM (based on tubulin dimer) in a co-sedimentation assay with KIF14. A representative gel from three independent experiments is shown.

microtubule-stimulated ATPase rate at each concentration, we had to normalize it to the high basal rate, which is not negligible especially at low microtubule concentrations. Therefore, the determined k_{cat} value 2.65 s^{-1} is an underestimate of the true value, which is approximately 3.5 s^{-1} based on the low saturating concentration of $\sim 0.3 \mu\text{M}$ tubulin dimers. This turnover rate is comparable to other mitotic kinesins such as Eg5 ($0.1\text{--}10 \text{ s}^{-1}$ [36,38,39]) but is much lower than the kinesin-3 motor KIF1A (110 s^{-1} [18]). However, GST-KIF14MD-D772's $K_{1/2, \text{MT}}$ value of $\sim 20 \text{ nM}$ is at least an order of magnitude lower than most kinesins (kinesin-1: $1.1 \mu\text{M}$ [35]; kinesin-5: $0.3\text{--}6.78 \mu\text{M}$ [36,40]) but is in the same range as KIF1A ($16 \pm 8 \text{ nM}$ [18]), implying that KIF14 associates tightly with microtubules. Interestingly, tubulin dimers also stimulated the ATPase rate of GST-KIF14MD-D772 to a similar level as microtubules did, albeit that the $K_{1/2, \text{MT}}$ value was higher ($0.33 \mu\text{M}$; Fig. 2c). We verified that this ATPase activity was indeed coming from the stimulation of tubulin dimers, and not microtubules, by both sedimentation of the reaction mixtures showing the absence of polymers and comparison with data obtained from GST-Eg5MD and MCAK-MD (both have very low tubulin dimer-stimulated activity but relatively high microtubule-stimulated activity; Fig. S3). Because of

KIF14's high basal ATPase activity, we next carried out an ATP titration under both non-stimulated and microtubule-activated conditions. From this we determined the basal $K_{\text{m,ATP}}$ of GST-KIF14MD-D772 to be $62 \mu\text{M}$ and that of the stimulated $K_{\text{m,ATP}}$ to be $33 \mu\text{M}$ (Fig. 2d). This slight decrease in $K_{\text{m,ATP}}$ value in the presence of microtubules may reflect the enhancement in ATP turnover via microtubule binding. Taken together, these data show that the KIF14 motor domain has a robust ATPase activity with unusually high basal and tubulin dimer-stimulated activities.

KIF14 motor domain has high affinity to microtubules

It should be noted that the ionic strength we used in our ATPase assays (40 mM Pipes + 75 mM KCl) is higher than the buffer conditions traditionally used for kinesin-1 or kinesin-5 (from 12 mM Pipes to 80 mM Pipes with $0\text{--}20 \text{ mM}$ KCl [35,37–39]). Normally, this would increase the saturating microtubule concentration required for $K_{\text{m,ATP}}$ determination, but the high microtubule affinity of GST-KIF14MD-D772 appears to make it less sensitive to ionic strength changes that perturb electrostatic interactions between other kinesins and microtubules [41,42]. To

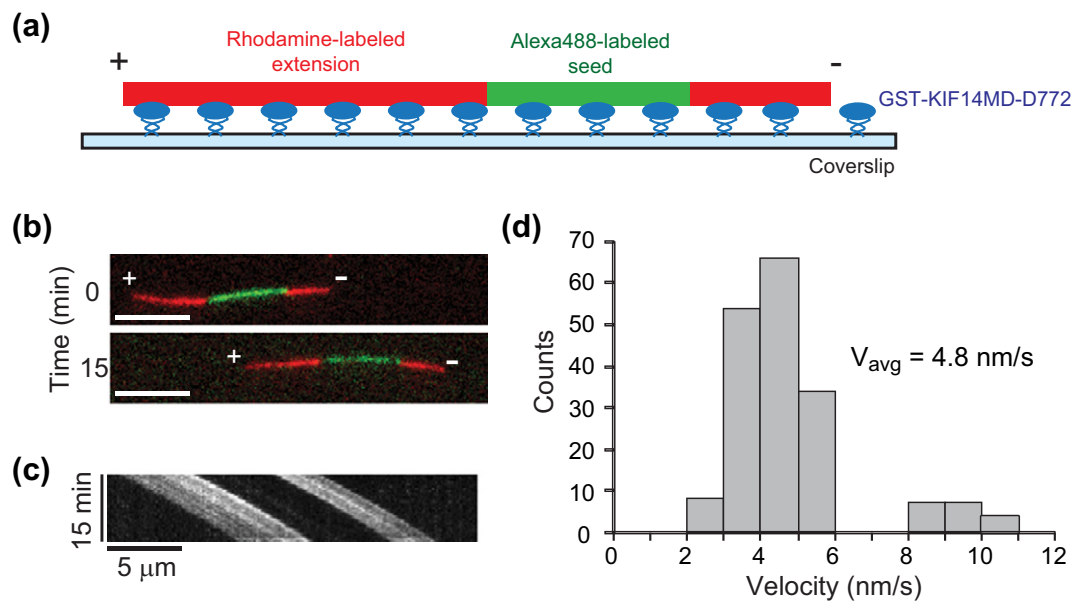


Fig. 4. KIF14 is a plus-end-directed motor. (a) An illustration depicting a microscopy-based, GST-KIF14MD-D772-driven microtubule-gliding assay. (b) Two frames of a time-lapsed recording are shown with the assigned plus (+) and minus (–) ends of microtubules indicated. The bar represents 5 μm. (c) Corresponding kymograph of the microtubule shown in (b). (d) Velocity distribution of GST-KIF14MD-D772 on microtubules with distinguishable short and long extensions. Of the motile polarity-marked microtubules, only 7 out of the 180 were moving in the wrong direction (with the long extension leading). It should be noted that all microtubules with a velocity over 8 nm/s came from one time-lapse recording (1 out of 11 recordings).

substantiate this further, we measured ATPase turnover rate of GST-KIF14MD-D772 in comparison to a GST fusion construct of the Eg5 motor domain (GST-Eg5MD) at KCl concentrations ranging from 0 to 200 mM (Fig. 2e). We observed that GST-KIF14MD-D772 was more resistant to high ionic strength, showing robust ATPase turnover even at 125 mM KCl (2.70 s^{-1} , >85% of its maximal rate). In contrast, the ATPase rate of GST-Eg5MD dropped below 25% at 75 mM and to virtually 0 at KCl concentrations above 100 mM.

The low $K_{1/2,MT}$ of GST-KIF14-MD-D772 suggests that KIF14 has an unusually high affinity to microtubules among kinesins, and we were curious about how this affinity changes during the ATP hydrolysis cycle. The ADP-bound state is the weaker binding state for most motile kinesins [43–45]. This allows the motor head to release from microtubules and couple microtubule binding–unbinding steps with ATP turnover. To explicitly evaluate the nucleotide-dependent microtubule binding affinity of KIF14MD, we performed co-sedimentation assays in the presence of ADP or AMPPNP (a non-hydrolyzable ATP analog) with KIF14MD-D772. This construct was used in order to eliminate the complication of artificial dimerization by GST. We found that KIF14MD-D772 co-pelleted completely with microtubules under both conditions (Fig. 3a) and that the binding affinity in the presence of ADP or AMPPNP was indistinguishable. This is in

direct contrast to prototypical kinesins such as Eg5 (using non-GST-tagged Eg5MD), which dissociate from microtubules upon conversion to the ADP-bound state (Fig. 3b). To get a better estimate on the dissociation constant of KIF14MD-D772-binding to microtubules, we titrated the microtubule concentrations down to 62.5 nM in the presence of ADP. Even at this very low level, we found that nearly all of the KIF14MD-D772 protein co-pelleted with microtubules, indicating that the K_d is lower than 62.5 nM (Fig. 3c). These data demonstrate that the microtubule binding affinity of KIF14 is less sensitive to nucleotide exchange than most kinesins. This property can also be observed for the two shorter constructs used in this paper (KIF14MD-L735 and KIF14MD-N738; Fig. S2b and c), suggesting that it is inherent to the motor domain. However, comparison of the amount of pelleted kinesin at the 0.06 μM tubulin concentration for each construct (Fig. 3c and Fig. S2c) indicates that the neck linker also contributes to this high binding affinity. It should also be noted that KIF14MD's high affinity to microtubules is molecularly distinct from KIF1A since KIF14 does not possess the consecutive series of positively charged lysine residues on the K-loop found in KIF1A and, to a lesser extent, in other forms of kinesin-3 (Fig. 1b). This region has been proposed to help KIF1A maintain microtubule contact during the weak binding state via interaction with the C-terminal glutamate-rich E-hook of tubulin [18].

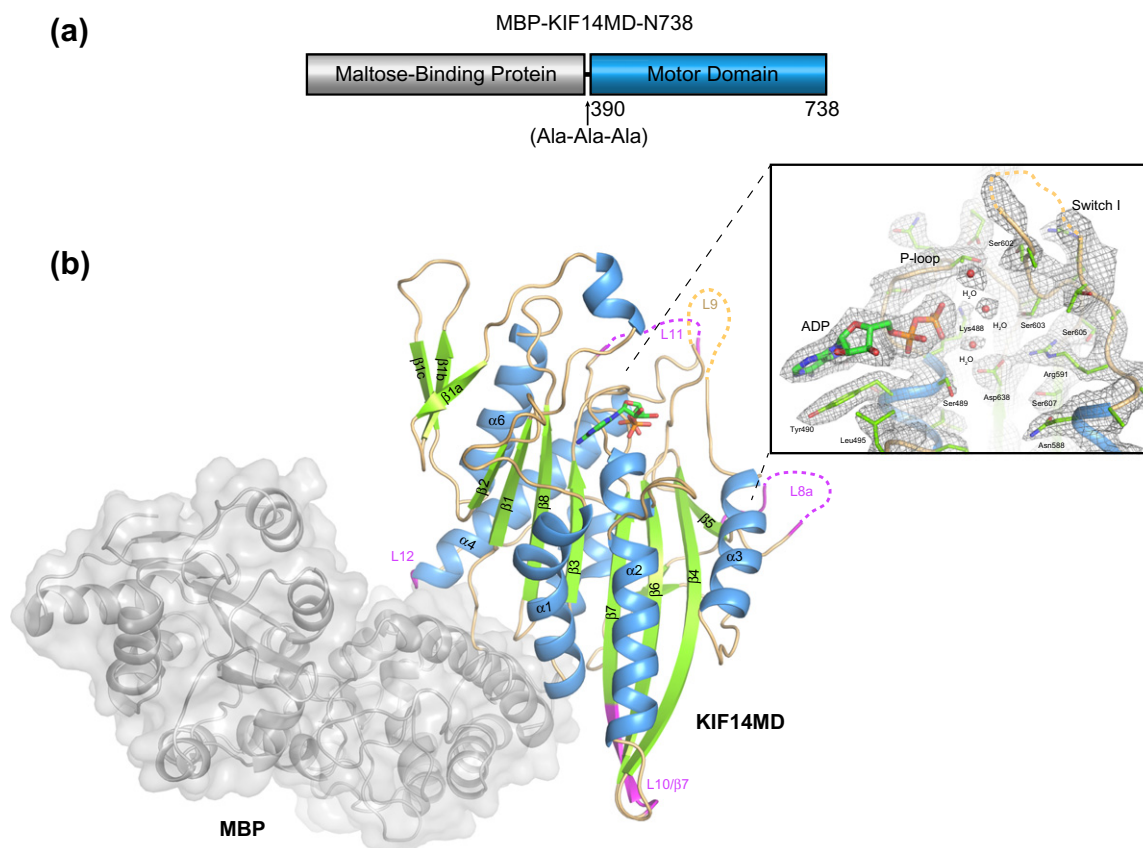


Fig. 5. The structure of MBP-KIF14MD. (a) A schematic of the MBP-KIF14MD-N738 fusion construct displaying the polyalanine linker and the boundaries of the mouse KIF14 motor domain used for crystallization. (b) Ribbon representation of the structure of KIF14MD-N738 (in blue and green) fused to MBP (in gray). Regions of the motor domain that show major sequence divergence from other kinesins are highlighted in purple in loops L8a, L10, and L12, as well as β 7. The inset panel shows the nucleotide-binding pocket of KIF14MD modeled within electron density from a $2mF_o - DF_c$ map contoured at 1.0σ . The figure was created using PyMOL [93].

KIF14 is a slow plus-end-directed motor

KIF14 is a kinesin-3 motor that has a unique extension N-terminal of the motor domain, which places the motor domain in the middle of the protein (Fig. 1a). Despite this extension, KIF14 is classified as an N-terminal kinesin (or Kin-N) and not an internal motor domain kinesin (or Kin-I such as kinesin-13 proteins) because it has a neck linker motif C-terminal to its motor domain. On this basis, it is expected to move toward the microtubule plus end, but this has not been confirmed. Given the robustness of GST-KIF14MD-D772 in hydrolyzing ATP, we next determined its motile activity in a microscopy-based microtubule-gliding assay using polarity-marked microtubules with surface-absorbed motors (Fig. 4a). We observed that nearly all of the microtubules moved with their minus ends leading (173 out of 180 microtubules with unambiguously distinguishable ends) (Fig. 4b). Therefore, we conclude that KIF14 is indeed a plus-end-directed motor, as predicted by the location of the neck linker

relative to the motor domain. However, we found that GST-KIF14MD-D772 has an average gliding velocity of 4.8 nm/s (Fig. 4c), which is approximately three times slower than Eg5 and more than 200 times slower than the kinesin-3 motor KIF1A [17,38]. We also repeated the microtubule-gliding assay using GST antibodies as surface anchors and obtained an average velocity of 6.9 nm/s (Fig. S4), suggesting that the slow motility of KIF14MD was inherent to the motor and independent of the attachment methods. While these data indicate that KIF14 is a slow plus-end-directed motor, it must be cautioned that the GST-KIF14MD-D772 protein is still a truncated construct and therefore it is possible that our velocity measurements deviate from the actual speed of the full-length motor in cells.

Structure of the KIF14 motor domain

To complement our characterization of the biochemical and microtubule-binding properties of mouse KIF14, we determined the X-ray crystal

Table 1. Data collection and refinement statistics

MBP-KIF14MD-N738	
<i>Data collection statistics</i>	
Space group	<i>P</i> 1
Cell dimensions	
<i>a</i> , <i>b</i> , <i>c</i> (Å)	65.7, 73.6, 96.5
α , β , γ (°)	74.4, 87.4, 89.9
Resolution (Å) ^a	30–2.8 (2.9–2.8)
Total reflections	123,026
No. of unique reflections	40,225
<i>R</i> _{merge} ^a	13.3 (57.8)
<i>I</i> / <i>σ</i> ^a	10.72 (2.55)
Completeness (%) ^a	94.6 (93.9)
Redundancy ^a	3.1 (2.9)
<i>Refinement statistics</i>	
<i>R</i> _{work} / <i>R</i> _{free} ^b (%)	26.38/30.75
No. of atoms	
Protein (chain A)	5070
Protein (chain B)	5096
Water	36
Average <i>B</i> -factors (Å ²)	
Protein (chain A)	49.87
Protein (chain B)	48.24
Nucleotide (A)	17.72
Nucleotide (B)	18.45
Water	18.75
RMS deviations	
Bond lengths (Å)	0.011
Bond angles (°)	1.47
Ramachandran plot (%)	
Favored	89.6
Allowed	10.0
Generously allowed	0.4
Disallowed	0.0

^a Data in parentheses represent the highest-resolution shell.

^b $R_{\text{factor}} = \sum |F_o - F_c| / \sum |F_o|$, where *R*_{work} refers to the *R*_{factor} for the data utilized in the refinement and *R*_{free} refers to the *R*_{factor} for 5% of the data that were excluded from the refinement.

structure of its motor domain (KIF14MD-N738) by fusing MBP to its N-terminus via a short polyalanine linker (Fig. 5a). This strategy readily gave crystals of suitable quality for diffraction data collection. The structure of MBP-KIF14MD-N738 was solved by molecular replacement using the coordinates for periplasmic MBP (PDB ID: 2R6G) [46] and the motor domain for KIF13B (PDB ID: 3GBJ) and was refined to 2.7 Å. Data collection and refinement statistics are summarized in Table 1. The asymmetric unit contained two MBP-KIF14MD-N738 molecules in which the MBP and KIF14MD-N738 components exist as distinct domains and form few intramolecular contacts (Fig. 5b). The main region of interaction between MBP and the motor domain involves part of loop L12 at the C-terminal end of helix α 4. Interactions between symmetry-related molecules in the crystal lattice are minimal as well and do not appear to impact the overall configuration of KIF14MD-N738. These involve the top of the β 1 lobe, the C-terminal end of helix α 2, and part of the microtubule-binding surface (β 5a, loop L8, and β 5b) of KIF14. The final electron density map allowed for

the building of residues Glu390–Arg734 in both molecules A and B, with small sections of some surface loops missing from the final model due to missing or ambiguous electron density. This includes loops L8a, L10, L11, and L12, which, along with part of β 7, is where KIF14 sequence differs most dramatically from other kinesin-3 family members (Fig. 1b). ADP, but not Mg²⁺, is found in the nucleotide pocket of both KIF14 molecules and the final refined structure shows that KIF14MD-N738 adopts the canonical α/β kinesin motor domain fold involving an eight-stranded β -sheet core sandwiched by three exposed α -helices on either side [42,47].

The nucleotide pocket

Secondary structure matching analysis by PDBeFold [48] shows that KIF14MD-N738 shares highest overall similarity with the Mg·ADP-bound structures of the KIF1A (PDB ID: 2ZF1) [25] and Eg5 (PDB ID: 1I16) [49] motor domain. Their RMS deviations for 253 and 229 structurally equivalent α -carbons are 1.018 Å and 1.041 Å, respectively. The greatest structural deviation exhibited by KIF14MD-N738 resides within the nucleotide-binding pocket. A profound picture of these differences emerges from superimposing their P-loop elements (residues 482–489 in KIF14: “GPQTxxGKS/T”) and highlighting their central β -sheet strands (Fig. 6a and b). While their nucleotide atoms and β 1, β 2, β 3, and β 8 strands (those on the P loop–switch II side) show appreciable overlap, the remainder of KIF14's central β -sheet (β 4– β 7, on the switch I side) is twisted an additional 8–11° beyond the maximal amount observed in KIF1A (Fig. 6a) and Eg5 (Fig. 6b). Along with this twist, helix α 3 and switch I are shifted away from the nucleotide-binding pocket to a distance of 8.7 Å as determined by measuring from Ser603 of the switch I “NxxSSR” motif to the β -phosphate of ADP (Table 2 and Fig. 6d). The result of this is near total loss of protein contacts for waters that mediate interactions with the nucleotide. Likewise, the conserved P-loop residue Lys488 (GPQTxxGKS/T) is further away from the β -phosphate of ADP in KIF14MD-N738 in comparison to KIF1A (PDB IDs: 2ZFM and 2ZF1) and Eg5 (PDB ID: 1I16) (Table 2).

A new intermediate state of the kinesin motor domain

Although open conformations of the nucleotide-binding pocket have been reported for other kinesin structures determined by X-ray crystallography [50] and high-resolution cryo-EM [24], the degree of central β -sheet distortion in KIF14MD-N738 has only been observed in nucleotide-free myosins V and II (Fig. 6c) [27,28]. This conformation has been described

in myosin as the “rigor-like” state of the motor, which resembles the strong actin-binding state that occurs at the end of a power stroke [51,52]. In kinesin, transition to this state has been presumed to result from stable microtubule lattice binding and is thought to trigger a fully opened conformation of switch II that completely releases Mg²⁺ and ADP [33]. Indeed, twisting of the central sheet of KIF14 appears to disrupt the “Mg²⁺-stabilizer” complex previously described in KIF1A structure [25]. Its purpose is presumed to hold the “Mg²⁺-water cap” in place to keep ADP in the nucleotide-binding pocket [20]. In KIF14, this complex is composed of residues Glu531_{L7}, Arg591_{swl}, and Asp638_{swl}, based on homology to KIF1A. While Asp638_{swl} and Arg591_{swl} maintain a hydrogen bond, Arg591_{swl} shifts away from Glu531_{L7} (Fig. 6d). Similar interactions are seen in KIF1A ADP-bound structure (PDB ID: 2ZFM) [25], in which the hydrogen bond is broken between Glu148_{L7} and Arg203_{swl}. As a consequence, KIF14MD-N738 contains no Mg²⁺, and only three water molecules in proximity of the phosphate groups of ADP, one of which connects switch II to β-phosphate by forming a weak hydrogen bond with Asp638_{swl}. Although the resolution of our structure approaches the limit for accurate modeling of water molecules and could therefore explain limited water occupancy, the B-factors for these atoms are roughly equivalent to the other waters (~19 Å²).

Another unique feature of the KIF14MD-N738 structure is that the side-chain orientation of the conserved serine of the P-loop (Ser489_{P-loop}, G_PQTxxGKS/T) does not allow for Mg²⁺ coordination nor can it form a hydrogen bond with the β-phosphate of ADP (Fig. 6d). In all KIF1A crystal structures, the homologous serine (Ser104_{P-loop}) exhibits an orientation that allows it to either coordinate the Mg²⁺ in the Mg·AMPPCP (PDB ID: 1I6I) [53], Mg·AMPPNP (PDB ID: 1VFV) [23], and Mg·ADP complexes (PDB ID: 2ZFI) [25] or interact with β-phosphate of the ADP complex (PDB ID: 2ZFM) [25]. This is also the case for the corresponding Thr112_{P-loop} residue in Eg5 (PDB IDs: 3HQD and 1I16) [49,54].

The KIF14MD-N738 structure also differs from some nucleotide-specific conformations of KIF1A in terms of the orientation of helix α4 of the switch II cluster. In ADP-bound KIF14MD-N738, helix α4 is in the “ADP-like” or “down” conformation [23,53,55], which prohibits docking of the neck linker onto the catalytic core. Nitta *et al.* observed this orientation of helix α4 in the KIF1A-Mg·ADP complex (PDB ID: 2FZI) (Fig. 6e) and proposed it to represent a predecessor to the Mg²⁺-release state [25]. In this state, the motor domain would be presumed to exhibit weak microtubule binding, which contradicts the microtubule affinity expected for the rigor-like conformation of KIF14's central sheet. Rather, in the model proposed by Nitta *et al.* to explain microtubule activation of Mg·ADP release from kinesin, rotation

of helix α4 to an “up” conformation, as seen in its ADP-bound KIF1A structure (PDB ID: 2ZFM) (Fig. 6e) [25], as well as the Mg·AMPPNP and Mg·AMPPCP-bound structures (PDB IDs: 1VFV and 1I6I) [23,53], was correlated with strong microtubule affinity [25]. The conformation of helix α4 in ADP-bound KIF14 is clearly different from these latter KIF1A structures.

Furthermore, the network of interactions described previously in KIF1A as the “tri-residue complex” (Tyr150_{L7}, Glu267_{L11}, and Arg216_{swl}) [25] is most similar in the KIF1A-Mg·ADP and the KIF14MD-N738-ADP complexes. Nitta *et al.* noted that these residues form hydrogen bonds that act as a “latch” to allow helix α4 to maintain a post-hydrolysis position (Fig. 6f). Upon Mg²⁺ release, a slight downward movement of loop L7 was seen in the ADP-bound model (PDB ID: 2ZFM) that appeared to break the latch, causing helix α4 to rotate toward the “up” conformation [20]. Cryo-EM studies with KIF1A, as well as KIF5 and Kar3, suggest that this movement of loop L7 does indeed occur on microtubules [24,56,57]. In comparison to KIF1A and Eg5, loop L7 of KIF14MD is rotated downwards significantly, and yet the corresponding three residues—Tyr533_{L7}, Arg604_{swl}, and Glu657_{L11}—maintain the latch with Tyr533_{L7} forming a strong hydrogen bond with Glu657_{L11}. Presumably, this helps hold helix α4 in the “down” position and could be the result of the additional twist in the central β-sheet as it affects all the elements participating in latch formation: loop L7, switch I, and loop L11.

While these relationships between the helix α4 conformation and nucleotide state of KIF1A make the KIF14 conformation seem paradoxical, other kinesin crystal structures show a range of helix α4 positions that bear little to no correlation to nucleotide identity. For example, crystal structures of KIF2C (PDB IDs: 1V8J and 1V8K) show the “down” helix α4 conformation in the presence of both ADP and AMPPNP in the nucleotide-binding pocket [58]. This most assuredly stems from the necessary absence of their microtubule substrate during crystallization [59]. By virtue of their microtubule association, EM studies seem to provide a more reliable depiction of nucleotide-dependent states of helix α4. In high-resolution 3D (3-dimensional) helical reconstructions of microtubule-bound kinesin-1 and kinesin-5, helix α4 of the switch II cluster is in the “down” conformation in rigor states (ADP and nucleotide-free) of these motors, similar to KIF14 [56,60]. Alternatively, the “up” conformation of helix α4 is attained in the presence of AMPPNP, and the neck linker is docked to the motor core [60]. Based on this, the conformation of KIF14 observed in the crystal structure may resemble its true microtubule-bound rigor-like state in which the neck linker is prevented from docking onto the core of the motor domain.

Also worth noting is that loop L7 has been identified as the pivot for both the “latch” and “Mg²⁺-stabilizer” complexes due to its role as the microtubule sensor. Two charged residues, located

at the tip of loop L7 (Glu535 and Lys536 in KIF14) are predicted to form salt bridges with Arg158 and Glu159 in helix H4 of β -tubulin, bringing loop L7 closer to β -tubulin [20]. Due to the intrinsic twist in the

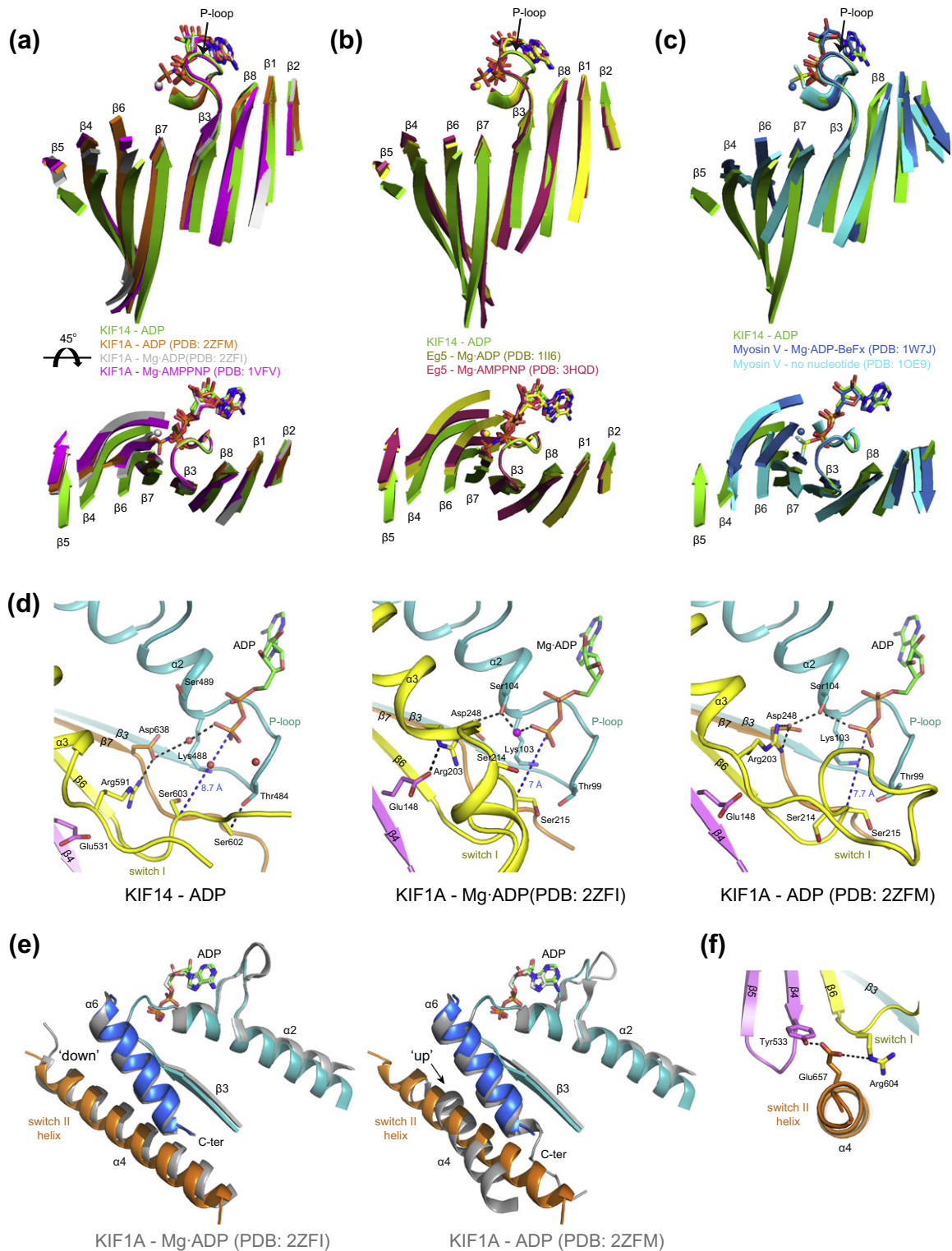


Table 2. Distances between nucleotide-binding motif elements in KIF14, Eg5, and KIF1A

Kinesin	PDB code	Nucleotide state	Salt bridge	Distance (Å)	Distance (Å)	Distance (Å)
				(β-phosphate–S _{swi}) ^a	(G _p –G _{swi}) ^b	(β-phosphate–K _{P-loop}) ^c
KIF14	4OZQ	ADP	No	8.71 (S603)	6.02 (G482–G641)	3.6
Eg5	3HQD	AMPPNP	Yes	6.41 (S233)	5.37 (G105–G268)	3.8
Eg5	1II6	ADP	Imperfect	7.13 (S233)	5.97 (G105–G268)	2.8
KIF1A	2ZFM	ADP	R216 side chain missing	7.66 (S215)	5.91 (G97–G251)	2.9
KIF1A	2ZFI	ADP	No	6.98 (S215)	5.81 (G97–G251)	2.7
KIF1A	1VfV	AMPPNP	Imperfect	7.74 (S215)	5.52 (G91–G251)	3.4
KIF1A	1I6I	AMPPCP	No	8.02 (S215)	5.89 (G91–G251)	4.0

Emsley P, Cowtan K. Coot: model-building tools for molecular graphics. *Acta Crystallogr Sect D Biol Crystallogr* 2004;60:2126–32.

^a Distance between β-phosphate and the second serine in the switch I motif NxxSSR (S_{swi}).

^b Distance between the first glycine in the P-loop motif GPQTxxGKS/T (G_p) and the conserved glycine in the switch II motif DxxGxE (G_{swi}).

^c Distance between β-phosphate and the lysine in the P-loop motif GPQTxxGKS/T (K_{P-loop}). Distances were measured from the α-carbons of the indicated residues using the program Coot [82]. Each of these distances were used as a measure of the closure of the nucleotide-binding pocket.

central β-sheet of KIF14, loop L7 and other parts of the microtubule-binding region (helix α4, β5a/b, and loop L8) are pulled closer toward the microtubule surface than is seen in other kinesins. This includes the recent crystal structure of kinesin-1 in complex with an α/β tubulin dimer [61]. There, the tubulin dimer was curved ~9° with respect to a linear microtubule. This suggests that the KIF14 crystal structure exhibits a conformation with steric complementarity to a straight microtubule protofilament. Its ability to achieve this conformation in the absence of tubulin might explain KIF14's strong microtubule-binding affinity in the ADP-bound state.

KIF14 can stabilize microtubules against cold-induced depolymerization *in vitro*

We hypothesized that KIF14MD's rigor-like microtubule-binding characteristic would be well suited for stabilizing microtubules at the spindle midzone or midbody. To demonstrate its ability to protect microtubules from depolymerization and further distinguish KIF14 from other mitotic kinesins such as Eg5, we developed an *in vitro* reconstitution assay that assesses inhibition of cold-induced microtubule disassembly. In this assay, taxol-stabilized microtubules were diluted into a low taxol

and low tubulin concentration regime in the presence or absence of KIF14MD-D772 and Eg5MD and were subjected to low temperature (2 °C) to induce depolymerization. A saturating concentration of ATP was used in the reaction to mimic the high ATP concentration in cells. After normalizing the level of cold-induced depolymerization to the control sample without kinesin, we found that KIF14MD-D772, but not Eg5MD, effectively protected microtubules from cold-induced depolymerization (Fig. 7). We attribute KIF14MD-D772's microtubule stabilizing effect, at least in part, to its high binding affinity to microtubules and to the limited effect of nucleotide exchange on this affinity.

EM of KIF14–microtubule complexes

To gain insight into how KIF14 motor interacts with microtubules, we analyzed the structure of KIF14MD–microtubule complexes using cryo-EM (Fig. 8). We chose to use the untagged KIF14MD-L735 construct for this experiment because of its similar length to MBP-KIF14MD-N738, but without the complication of a tag. We incubated microtubules with saturating amounts of KIF14MD-L735 in the presence of the non-hydrolyzable ATP analog AMPPNP. Under these conditions,

Fig. 6. The conformational changes in KIF14MD. (a and b) Superposition of the α-carbon atoms of the P-loop indicates a twist of the central β-sheet in MBP-KIF14MD-N738 when compared to selected crystal structures of KIF1A and Eg5, respectively. (c) Distortion of the central β-sheet of MBP-KIF14MD-N738 is similar to that observed in myosin V upon transitioning from an ATP-bound state to a nucleotide-free state [27]. (d) The open state of the nucleotide-binding pocket of KIF14 in comparison to the Mg·ADP-bound and ADP-bound states of KIF1A. Black broken lines show hydrogen bonding interactions. The blue broken line shows a measurement of the distance between the nucleotide and switch I as determined by measuring from the second conserved serine of the switch I “NxxSSR” motif to the β-phosphate of ADP. Also shown are the interactions between residues that compose the “Mg²⁺-stabilizer” complex. In KIF14, this complex is composed of residues Glu531, Arg591, and Asp638, based on homology to KIF1A. (e) Left panel shows an overlay of MBP-KIF14MD-N738 helix α4 on the KIF1A structure just prior to Mg²⁺ release (PDB ID: 2ZFI), which exhibits the “down” conformation of α4 [25]. Right panel shows MBP-KIF14MD-N738 and the structure of KIF1A with helix α4 in the “up” conformation following the release of Mg²⁺ (PDB ID: 2ZFM) [25]. (f) Illustration of residues that form the “latch” (Tyr533, Arg604, and Glu657).

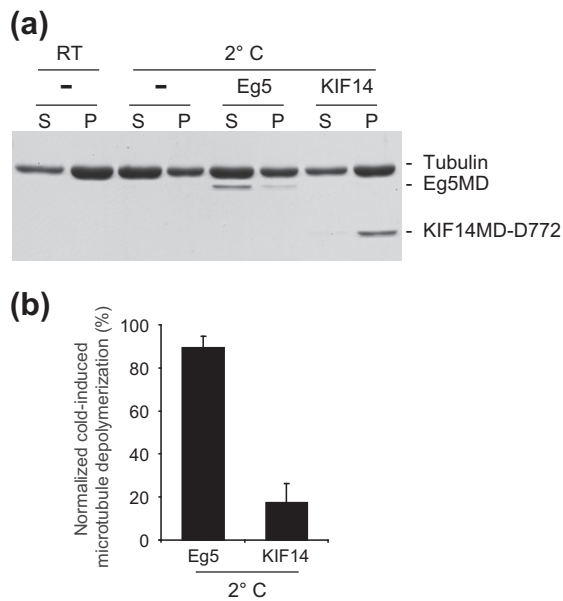


Fig. 7. KIF14 motor domain protects microtubules from cold-induced depolymerization. Microtubules mixed with buffer alone (–) or with the indicated kinesin motors (Eg5MD or KIF14MD-D772) were subjected to the indicated temperatures for 30 min, followed by sedimentation via ultracentrifugation to monitor the state of microtubule polymers. (a) Supernatant (S) and pellet (P) fractions of each sample were resolved by SDS-PAGE and the gel was stained by Coomassie blue. (b) Percentage of cold-induced depolymerization, normalized to control sample at room temperature (as 0%) and at 2°C (as 100%), is shown (averaged from four experiments). Error bars represent standard deviations.

the KIF14MD-L735 binds to each tubulin heterodimer resulting in fully “decorated” microtubule complexes (Fig. 8a). We calculated a 1.6-nm-resolution 3D map of the complex (Fig. 8b and Fig. S5) and fitted the KIF14MD-N738 and tubulin atomic structures into the map (Fig. 8c and d). The 3D map and fitted atomic model reveals an overall binding configuration similar to other kinesins [62]. KIF14MD-L735 binds at the tubulin intradimer interface, at the crest of the protofilament, and orients slightly toward the next protofilament resulting in the typical clockwise slew when the complex is viewed from the microtubule plus end. Comparing the KIF14MD-L735-microtubule model with other kinesin–microtubule models [24] revealed a small difference in the position/orientation of the KIF14MD relative to tubulin (Fig. 8d). This distinct binding configuration may be a direct consequence of a different KIF14MD structure.

Nucleotide-dependent changes in the orientation and position of kinesin elements involved in microtubule binding, such as helix $\alpha 4$, are associated with changes in the position of the bulk of the motor domain in kinesin–microtubule complexes [24,63,64]. KIF14 helix $\alpha 4$ may adopt a configuration

in the microtubule-bound ATP state (as mimicked by AMPPNP) that is different from other kinesins, resulting in the distinct position/orientation we see in the microtubule complex 3D map. A higher resolution 3D map would be needed to confirm this by showing rearrangements of specific secondary structure elements. However, the cryo-EM and crystallography data together strongly indicate that, compared to other kinesins, KIF14MD exhibits unique conformations associated to each ATPase cycle step. This appears to result in a tight microtubule interaction through the whole cycle. We also propose that the distinct binding configuration of the KIF14MD relative to the microtubule may be associated with the observed microtubule stabilizing effect.

Discussion

Here we presented a biochemical and structural characterization of the mitotic motor KIF14. As a kinesin-3 family member, it is perhaps not surprising that KIF14 shows some similarities to KIF1A, including its high affinity to microtubules. However, there are also several striking differences that are highlighted by our biochemical and structural studies. For example, KIF14 is an extremely slow and inefficient walking motor compared to KIF1A, which runs at more than 200 times faster (1200 nm/s) than KIF14 (5 nm/s) [17]. With an ATPase rate of $\sim 110 \text{ s}^{-1}$, KIF1A hydrolyzes about 1 ATP per 8 nm step similar to the conventional kinesin, kinesin-1 [37,65]. By our calculation, KIF14 makes one step every 2 s but hydrolyzes about 7 ATP molecules during this period of time. This implies that futile hydrolysis occurs in the mechanochemical cycles of KIF14. Although it remains to be determined whether this is a consequence of KIF14's high basal ATPase activity or loss of coordination between KIF14 heads as a consequence of using truncated motors, we propose that the former explanation is more likely. This is due to the proclivity of KIF14MD to adopt a wide-open nucleotide-binding pocket and high microtubule affinity conformation in the absence of microtubules, as demonstrated in the crystal structure. Such ability should accelerate the process of ADP release and ATP entry. The limited activation of ATP turnover in the presence of microtubules suggests that closing of the switch elements around ATP occurs readily without microtubules as well. Furthermore, the miscoordination between the nucleotide states and the conformation of the motor core and microtubule binding elements in KIF14 and KIF1A crystal structures may also explain some of the differences in the rate and equilibrium constants of their mechanochemical cycles and microtubule interactions. These distinctions provide a logical explanation for the divergent

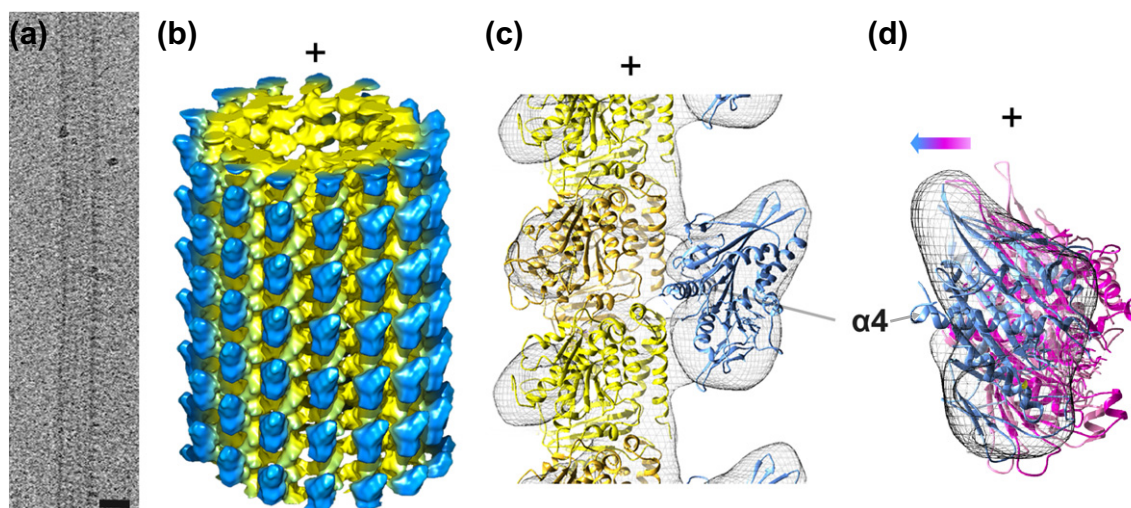


Fig. 8. KIF14 motor domain microtubule complex cryo-EM 3D reconstruction. (a) Cryo-EM image of a 15-protofilament microtubule decorated with KIF14MD-L735. (b) Surface representation of the 3D reconstruction density map colored according to radial position and protein identity. Yellow: tubulin; blue: KIF14MD. The 3D reconstruction Fourier shell correlation (FSC) curve is shown in Fig. S5. (c) Atomic structure of the KIF14 motor domain (blue ribbon) and tubulin (yellow: α -tubulin; ochre: β -tubulin; PDB ID: 1JFF) fitted into the cryo-EM density map (black mesh). (d) Fitted model viewed from the microtubule surface. The tubulin structure is clipped away and only the KIF14MD (blue ribbon) is shown. For comparison with other kinesin-microtubule complexes, the tubulin part of the KIF14-microtubule complex was superimposed with the tubulin part of two KIF1A microtubule complexes [light pink, KIF1A-MT in AMPPNP (PDB ID: 2HXF); dark pink, KIF1A-MT in ADP (PDB ID: 2HXH)] [24]. When aligned this way, the KIF14 motor domain is slightly displaced relative to the motor domains of the KIF1A-microtubule complex models, as indicated by the colored arrow. The scale bar in (a) represents 25 nm; in (b-d), the microtubule is oriented with the plus end toward the top of the page.

physiological roles of these two kinesin-3 motors: KIF1A in organelle transport in neurons and KIF14 in conveying midbody functions during cell division.

The unexpected yet highly important outcome of this study is that the KIF14MD structure provides a missing link involved in understanding the mechanism of force generation in kinesins. Until now, twisting of the central β -sheet has only been observed in the nucleotide-free form of evolutionarily related motor myosin [27,28]. This rearrangement causes the actin-binding cleft in myosin to close, leading to a marked increase in actin affinity, as well as P_i and ADP release. Conversion of the motor to the strong actin-binding state is viewed to be the major contributor to the loss of free energy needed to perform the power stroke [33,66]. In this way, distortion of the central β -sheet provides the structural basis for communication between the actin-binding, nucleotide-binding, and force-producing subdomains [27]. In kinesin, translocation is produced upon binding to ATP and docking of the neck linker against the motor core when the motor is attached to the microtubule [53]. The recent crystal structure of kinesin-1 in complex with $\alpha\beta$ tubulin illustrated this relationship and showed a twist of the β -sheet that was only marginally more pronounced than that of free kinesin in complex with ADP [61]. Gigant *et al.* suggested this to mean that they had captured the remnant of an event involving a much

larger twist [61], that being kinesin's rigor state. We propose that this state, or an event immediately preceding this state, is observed in the KIF14 structure. Proceeding from this state, ATP binding presumably untwists the central β -sheet, leading to re-orientation of the bulk of the motor domain relative to the microtubule on the stationary helix $\alpha 4$, as depicted in the "seesaw" model [59,64,67]. Concomitant widening of the gap between helix $\alpha 4$ and the N-terminus of the motor domain would expose the neck linker docking position on the motor core, directing the C-terminal neck toward the microtubule plus end. Given that ADP remains bound to our KIF14 structure, perhaps the structure of nucleotide-free KIF14 will be required to establish if a more pronounced distortion of the central β -sheet accompanies nucleotide release. However, it is relevant to note that soaking rigor-like myosin V crystals with $Mg \cdot ADP$ produced an ADP-bound state with minimal alterations compared to the nucleotide-free structure [27].

Unfortunately, it is not obvious from inspection of the structure, or from consideration of the sequence of amino acids that comprise it, why KIF14 displays a more distorted central β -sheet than other kinesins. As previously noted, L8a, L10, L11, L12, and part of $\beta 7$ show some particularly unique regions of amino acid sequence compared to other kinesin-3 motors, and indeed, there are differences between KIF14

and KIF1A in the configuration of these regions where accurate atomic modeling was feasible. However, it is difficult to assert with confidence that these discrepancies form deformable linkages or favor unique interactions with subdomains of the motor that readily enable β -sheet distortion. In areas where the primary structure was more conserved, such as loops L3 and L5 and helices α 2b and α 3, we also see some 3D structure divergence, but again, their connection to the twisted conformation of the KIF14 motor core cannot be clearly delineated without targeted mutagenic studies. A likely, albeit imprecise, prediction is that many regions throughout the motor domain of KIF14 contribute to its ability to populate the rigor-like state in the absence of microtubules. What is clear is that KIF14 is not dissimilar from some isoforms of myosin, whose propensity for central β -sheet distortion and actin-binding cleft closure in the absence of actin is greater than other myosins [68]. Whether, like myosins [51], kinesins with different kinetic and functional properties access similar rigor-like conformations in the absence of microtubules remains to be shown.

Considering the presumed functions of KIF14 at the midbody during cytokinesis [7,8], its slow motility and limited sensitivity to changing nucleotides with respect to microtubule association may be important if its primary role is to organize and bundle adjacent midbody microtubules. This parallels Eg5's function in the mitotic spindle [69–72]. Having a motor that binds tightly to microtubules also appears to offer a functionality that facilitates microtubule stabilization. Therefore, KIF14 could act as an assembled array of motors in between microtubule bundles to generate a limited (distance-wise) but more powerful antiparallel sliding than Eg5. In this regard, the midzone or midbody microtubule system involving KIF14 may resemble more of a “mitotic muscle” than the mitotic spindle [73,74]. The biochemical and structural features of KIF14 that we present here provide a molecular basis for testing this hypothesis in the future.

Materials and Methods

Cloning, protein expression, and purification

KIF14_N391-L735 and KIF14_N391-D772 constructs were generated as GST-fusion proteins. KIF14 coding region were amplified by PCR and cloned into the pGEX-6P1 vector. To express the recombinant proteins, plasmids were transformed into BL21 pLys *Escherichia coli* cells. Transformants were grown in Luria–Bertani media and induced with 0.1–0.5 mM IPTG at 18 °C overnight. GST-fusion proteins were purified on glutathione resin (GE Healthcare) according to the manufacturer's protocol in lysis/binding buffer [20 mM Tris (pH 7.5), 250 mM NaCl, 0.1% Triton X-100, 1.5 mM MgCl₂, 0.5 mM

ATP, 1 mM β -mercaptoethanol, 1 mM PMSF, and 2 mM benzamidine HCl]. Resins were washed in the binding buffer (with 500 mM NaCl and 0.2 mM ATP). Proteins were either eluted with 5 mM reduced glutathione [in 50 mM Tris (pH 8.0), 150 mM NaCl, 1 mM MgCl₂, 0.2 mM ATP, and 1 mM DTT] to generate the GST-fusion or cleaved on beads with PreScission protease [in cleavage buffer: 20 mM Hepes (pH 7.2), 1 mM MgCl₂, 200 mM NaCl, 1 mM TCEP, and 0.2 mM ATP] to generate the untagged motors. Eluted GST-KIF14 constructs were dialyzed in storage buffer (1 \times BRB80, 150 mM KCl, 0.2 mM ATP, and 1 mM DTT) supplemented with 10% sucrose, flash frozen in liquid nitrogen, and stored in –80 °C freezer. The mouse KIF14_E390-N738 construct was amplified by PCR and cloned into pMal-MATa1 (Addgene) using HindIII and PstI for expression as an MBP fusion [75]. The resulting protein, MBP-KIF14MD-N738, was expressed in the BL21-Codon-Plus (DE3)-RIL *E. coli* cell line (Stratagene) in Luria–Bertani media supplemented with the appropriate antibiotics as previously described [76]. Cells were resuspended in Column Buffer [10 mM NaPO₄ (pH 7.2), 200 mM NaCl, 2 mM MgCl₂, 1 mM ethylene glycol bis(β -aminoethyl ether) *N,N*-tetraacetic acid (EGTA), 0.2 mM ATP, 5 mM β -mercaptoethanol, and ethylenediaminetetraacetic-acid-free protease inhibitors (Sigma-Aldrich)] and lysed on ice by sonication. Soluble protein was recovered by centrifugation at 21,000 rpm for 40 min in a Beckman JA-25.5 rotor, and the supernatant was loaded onto an amylose resin column (New England Biolabs) that had been equilibrated with Column Buffer. After thorough washing with 12 column volumes of Column Buffer, we eluted MBP-KIF14MD-N738 with Column Buffer supplemented with 10 mM maltose. Peak fractions containing purified MBP-KIF14MD were pooled and further purified by size-exclusion chromatography in 20 mM Hepes (pH 7.2), 1 mM MgCl₂, 150 mM NaCl, 1 mM TCEP, and 0.2 mM ATP. Final peak fractions from column chromatography were pooled and concentrated with Amicon Ultra concentrators (Millipore) and flash frozen in liquid nitrogen for storage at –80 °C. GST-Eg5MD and MCAK-MD (187–589) were purified as previously described [77]. Bovine brain tubulins and fluorescently labeled tubulins were prepared using standard protocols as previously described [78].

ATPase assay and kinetic analysis

All kinetic experiments were performed in 384-well plates using the malachite green-based phosphate detection assay. Malachite green reagent was prepared by dissolving 8.1 mM ammonium molybdate in 1 M HCl, to which 2.7 mM malachite green was added to obtain a saturating concentration; the reagent was then filtered to remove any insoluble materials. Individual reaction mixtures were usually assembled in a 30 μ l volume with the following composition: BRB40 [40 mM Pipes (pH 6.8), 0.5 mM EGTA, and 0.5 mM MgCl₂], 10 μ M taxol, 0.25 mg/ml casein, 1 mM DTT, 1 mM MgCl₂, and 0.02% Tween-20 with the indicated concentrations of KCl, ATP, microtubules, and kinesin motors. In general, reactions were assembled in the following way: A microtubule mix containing taxol-stabilized microtubules and ATP and an enzyme mix containing the rest of the reaction components were made separately. Reactions were initiated by combining the two mixtures and

were allowed to proceed for 10 or 15 min, within the linear portion of the reaction curve (Fig. S1), and then quenched with 30 μ l of 90 mM perchloric acid. We then added 30 μ l of the quenched mixture to 40 μ l malachite green reagent to develop the color. After 5- to 10-min incubation, the amount of phosphate generated in each well was quantified by measuring the absorbance at 620 nm using the Tecan Genios Plus plate reader. The amount of phosphate generated in each well was determined by the absorbance reading at 620 nm using a standardized calibration curve obtained from a phosphate titration in the reaction buffer (Fig. S1). Concentrations of KIF14MD constructs in the ATPase reactions used were as follows, unless stated otherwise: for tubulin dimer-stimulated or microtubule-stimulated activity: 15 nM for KIF14MD-D772 (GST or untagged), 60 nM for KIF14MD-L735, and 60 nM for MBP-KIF14MD-N738. The basal rate for each construct was determined either by a concentration titration or by a calculation from the reaction without tubulin/microtubules. K_m , $K_{1/2, MT}$, and k_{cat} values were determined by hyperbolic fits of the plots of turnover rates against substrate concentrations to the Michaelis–Menten equation using KaleidaGraph (Synergy).

Crystallization, data collection and processing, and structure determination

Crystals of the MBP-KIF14MD-N738 fusion grew by hanging-drop vapour diffusion at 4 °C after mixing protein (28 mg/ml) supplemented with 1 mM Mg·ATP in a 1:1 volume ratio with a solution of 200 mM sodium formate (pH 7.0) and 12% polyethylene glycol 3350. Rod-like crystals appeared overnight and were flash frozen in cryoprotectant composed of 15% polyethylene glycol 3350, 300 mM sodium formate (pH 7.0), and 25% (v/v) ethylene glycol.

X-ray diffraction data were collected from a single frozen crystal on the X6A beam line at the National Synchrotron Light Source Facility (Brookhaven National Laboratory, New York) and were integrated and scaled with the program HKL2000 [79]. A molecular replacement search using the program BALBES [80] identified coordinates KIF13B (PDB ID: 3GBJ) (unpublished results) and MBP (PDB ID: 2R6G) [46] as search models for Phaser [81]. A series of manual building cycles using Coot [82] and iterative restrained refinement cycles using non-crystallographic symmetry restraints and TLS refinement in REFMAC 5.7 [83] were performed to generate the final model. Data collection and refinement statistics are summarized in Table 1. Coordinates and structure factors have been deposited in the Protein Data Bank with accession number 4OZQ.

Microtubule co-sedimentation assay

Co-sedimentation assays were performed as previously described with some modifications [84]. Briefly, microtubules were prepared by polymerizing tubulin at 25–50 μ M in 1 \times BRB80 (80 mM Pipes, 1 mM EGTA, and 1 mM MgCl₂), 1 mM GTP, and 1 mM DTT in the presence of 10% DMSO at 37 °C for 30 min, then diluted to 10 or 20 μ M working stocks in 1 \times BRB80 with 20 μ M taxol. Binding reactions were performed by mixing the indicated

kinesin constructs with microtubules in 1 \times BRB80 supplemented with the indicated salt concentrations (25–75 mM NaCl), 1 mM DTT, 0.01% Tween-20, and 20 μ M taxol. After a 20-min incubation, mixtures were spun at 45,000–60,000 rpm in a Sorvall S120AT3 rotor at 25 °C for 5 min. Supernatant and pellet fractions were recovered, resuspended in Laemmli buffer, and resolved by SDS-polyacrylamide gel electrophoresis. Gels were then stained with Coomassie blue R250 dye, destained, and scanned with a digital scanner. Protein band intensities were quantified using ImageJ (National Institutes of Health).

Microtubule surface-gliding assay

KIF14 motile activity was measured in a surface-gliding assay with polarity-marked microtubules in a flow chamber assay as previously described [38,85]. Briefly, the flow chamber was made by adhering a coverslip to a glass slide using two parallel strips of water-resistant double-sided adhesive tape. Polarity-marked microtubules were prepared by polymerizing preformed Alexa-488-labeled GMP-CPP seeds in an elongation mix containing 1.5 μ M X-rhodamine-labeled tubulin in 1 \times BRB80 with 0.05 mM GMP-CPP (Jena Bioscience) and 1 mM DTT in a 37 °C circulating water bath for 1 h. To carry out the microtubule-surface-gliding assay, we non-specifically absorbed GST-KIF14MD-D772 (at ~0.1 mg/ml) onto the coverslip in the flow chamber. After surface blocking with casein (0.5 mg/ml in BRB80), polarity-marked GMP-CPP microtubules were flown into the chamber to be captured by the surface-anchored GST-KIF14MD-D772. Reaction mix containing 1 \times BRB80, 50 mM KCl, 0.5 mg/ml casein, 1 mM Mg·ATP, and 1 \times oxidation mix [22.5 mM glucose, 0.22 mg/ml glucose oxidase (Sigma G-2133), 0.036 mg/ml catalase (Sigma C-40), and 4 mM DTT] was then introduced into the chamber to initiate KIF14 motility. The movements of microtubules were captured by a time-lapse recording every 30 s for 20 min using a Zeiss Axio-Imager Z1 microscope equipped with a 63 \times 1.4 Plan-APOCHROMAT objective and a cooled CCD camera using the Zeiss AxioVision Rel. 4.8 software. Recorded TIFF images were then visualized and analyzed using MetaMorph (Molecular Devices), with the rates of KIF14-driven microtubule gliding determined by kymography.

Cold-induced microtubule depolymerization assay

Microtubules were prepared as described above and diluted to 20 μ M with 1 \times BRB80 containing taxol (final concentration = 20 μ M). To prepare reaction mix for cold-induced depolymerization, microtubule stock was further diluted 10-fold in 1 \times BRB80 with 2 μ M taxol and 75 mM NaCl in the absence or presence of KIF14MD-D772 or Eg5MD (residues 1–437). To induce microtubule depolymerization, the mixtures were incubated at 2 °C for 30 min in a PCR machine and the control sample at room temperature. The mixtures were then subjected to ultracentrifugation to separate the depolymerized tubulin dimers from microtubules as described above in the co-sedimentation assay. Supernatant and pellet fractions were prepared and analyzed the same way as described above.

Cryo-EM and helical 3D reconstruction

Taxol/DMSO polymerized microtubules [86] were incubated with KIF14MD-L735 in a 2:1 (kinesin:tubulin) stoichiometry in the presence of 2 mM AMPPNP (MP Biomedicals). We applied 4 μ l of this solution onto freshly glow discharged holey carbon grids (Quantifoil R2/100) blotted and flash frozen as previously described [87]. Frozen grids were imaged under low dose conditions with a nominal defocus range of 1–2.5 μ m on a Tecnai-20 cryo-electron microscope operated at 120 kV. Electron micrographs were recorded on a TVIPS F415 4K \times 4K camera at a nominal magnification of 50,000 \times (1.6 \AA pixel size). Images with 15 protofilaments helical microtubules were selected for 3D image reconstruction as were selected for further analysis. Helical 3D reconstruction was performed as previously described [88]. Briefly, we used a Fourier–Bessel method to obtain a preliminary 3D map. This map was used as an initial reference for 10 rounds of single particle and 3D reconstruction refinement. Final resolution (1.6 nm) was estimated using the FSC_{0.143} criteria calculated from two independently refined reconstructions each including half of the data set (Fig. S5) [89,90]. The final map included 30 filaments and 24,722 asymmetric units. 3D map visualization and fitting of the crystal structures into the map was performed using UCSF chimera [91]. For fitting, we calculated 1-nm-resolution models of the atomic structures of tubulin (PDB ID: 1JFF) and the KIF14MD (PDB ID: 4OZQ) after deleting the MBP domain and fitted them independently as rigid bodies into the cryo-EM electron density map using the global fit option of the UCSF Chimera [91] fitmap command.

Accession numbers

Coordinates and structure factors have been deposited in the Protein Data Bank with accession number 4OZQ. The EM 3D map has been deposited in the EMDataBank with accession code EMD-2609.

Acknowledgements

We thank Shuaiqi Guo and Qilu Ye for assistance with diffraction data collection and processing and the AECOM Analytical Imaging Facility for help with EM. This work was supported by funding from the Natural Sciences and Engineering Research Council of Canada (K.A.: Natural Sciences and Engineering Research Council of Canada Postgraduate Scholarships), the Canadian Institutes of Health Research (J.S.A.: MOP-97832; B.H.K.: MOP-97928), the Ontario Early Researcher Award program (to J.S.A.), and the USA National Institutes of Health (H.S.: National Institutes of Health grant R01-GM083338). J.S.A. holds a Canada Research Chair (Tier 2) in Structural Biology. B.H.K. is a recipient of the Fonds de Recherche du Québec–Santé Chercheure-Boursière Junior 1 Award and the Canadian Institutes of Health Research New Investigator Award. B.H.K. acknowl-

edges the support of The Institute for Research in Immunology and Cancer and IRICoR, which are supported in part by the Canadian Center of Excellence in Commercialization and Research, the Canada Foundation for Innovation, and the Fonds de Recherche du Québec–Santé.

Conflict of Interest Statement: The authors declare no competing financial interests.

Appendix A. Supplementary data

Supplementary data to this article can be found online at <http://dx.doi.org/10.1016/j.jmb.2014.05.030>.

Received 14 March 2014;

Received in revised form 28 May 2014;

Accepted 29 May 2014

Available online 17 June 2014

Keywords:

kinesin;
KIF14;
motor protein;
microtubules;
crystal structure

† K.A. and L.T. contributed equally to this work.

Abbreviations used:

EM, electron microscopy; MBP, maltose-binding protein; EGTA, ethylene glycol bis(β -aminoethyl ether) N,N'-tetraacetic acid.

References

- [1] Corson TW, Huang A, Tsao MS, Gallie BL. KIF14 is a candidate oncogene in the 1q minimal region of genomic gain in multiple cancers. *Oncogene* 2005;24:4741–53.
- [2] Bowles E, Corson TW, Bayani J, Squire JA, Wong N, Lai PB, et al. Profiling genomic copy number changes in retinoblastoma beyond loss of RB1. *Genes Chromosomes Cancer* 2007;46:118–29.
- [3] Kim TM, Yim SH, Shin SH, Xu HD, Jung YC, Park CK, et al. Clinical implication of recurrent copy number alterations in hepatocellular carcinoma and putative oncogenes in recurrent gains on 1q. *Int J Cancer* 2008;123:2808–15.
- [4] Szponar A, Zubakov D, Pawlak J, Jauch A, Kovacs G. Three genetic developmental stages of papillary renal cell tumors: duplication of chromosome 1q marks fatal progression. *Int J Cancer* 2009;124:2071–6.
- [5] Filges I, Nosova E, Bruder E, Tercanli S, Townsend K, Gibson W, et al. Exome sequencing identifies mutations in KIF14 as a novel cause of an autosomal recessive lethal fetal ciliopathy phenotype. *Clin Genet* 2013. <http://dx.doi.org/10.1111/cge.12301>.
- [6] Zhu C, Zhao J, Bibikova M, Levenson JD, Bossy-Wetzell E, Fan JB, et al. Functional analysis of human microtubule-based motor proteins, the kinesins and dyneins, in mitosis/cytokinesis using RNA interference. *Mol Biol Cell* 2005;16:3187–99.

- [7] Carleton M, Mao M, Biery M, Warren P, Kim S, Buser C, et al. RNA interference-mediated silencing of mitotic kinesin KIF14 disrupts cell cycle progression and induces cytokinesis failure. *Mol Cell Biol* 2006;26:3853–63.
- [8] Gruneberg U, Neef R, Li X, Chan EH, Chalamalasetty RB, Nigg EA, et al. KIF14 and citron kinase act together to promote efficient cytokinesis. *J Cell Biol* 2006;172:363–72.
- [9] Corson TW, Gallie BL. KIF14 mRNA expression is a predictor of grade and outcome in breast cancer. *Int J Cancer* 2006;119:1088–94.
- [10] Corson TW, Zhu CQ, Lau SK, Shepherd FA, Tsao MS, Gallie BL. KIF14 messenger RNA expression is independently prognostic for outcome in lung cancer. *Clin Cancer Res* 2007;13:3229–34.
- [11] Basavarajappa HD, Corson TW. KIF14 as an oncogene in retinoblastoma: a target for novel therapeutics? *Future Med Chem* 2012;4:2149–52.
- [12] Euteneuer U, McIntosh JR. Polarity of midbody and phragmoplast microtubules. *J Cell Biol* 1980;87:509–15.
- [13] de Pennart H, Houliston E, Maro B. Post-translational modifications of tubulin and the dynamics of microtubules in mouse oocytes and zygotes. *Biol Cell* 1988;64:375–8.
- [14] Houliston E, Maro B. Posttranslational modification of distinct microtubule subpopulations during cell polarization and differentiation in the mouse preimplantation embryo. *J Cell Biol* 1989;108:543–51.
- [15] Kapitein LC, Peterman EJ, Kwok BH, Kim JH, Kapoor TM, Schmidt CF. The bipolar mitotic kinesin Eg5 moves on both microtubules that it crosslinks. *Nature* 2005;435:114–8.
- [16] Kapitein LC, Kwok BH, Weinger JS, Schmidt CF, Kapoor TM, Peterman EJ. Microtubule cross-linking triggers the directional motility of kinesin-5. *J Cell Biol* 2008;182:421–8.
- [17] Okada Y, Yamazaki H, Sekine-Aizawa Y, Hirokawa N. The neuron-specific kinesin superfamily protein KIF1A is a unique monomeric motor for anterograde axonal transport of synaptic vesicle precursors. *Cell* 1995;81:769–80.
- [18] Okada Y, Hirokawa N. A processive single-headed motor: kinesin superfamily protein KIF1A. *Science* 1999;283:1152–7.
- [19] Rashid DJ, Bononi J, Triplet BP, Hodges RS, Pierce DW. Monomeric and dimeric states exhibited by the kinesin-related motor protein KIF1A. *J Pept Res* 2005;65:538–49.
- [20] Hirokawa N, Nitta R, Okada Y. The mechanisms of kinesin motor motility: lessons from the monomeric motor KIF1A. *Nat Rev Mol Cell Biol* 2009;10:877–84.
- [21] Hammond JW, Cai D, Blasius TL, Li Z, Jiang Y, Jih GT, et al. Mammalian Kinesin-3 motors are dimeric *in vivo* and move by processive motility upon release of autoinhibition. *PLoS Biol* 2009;7:e72.
- [22] Verhey KJ, Hammond JW. Traffic control: regulation of kinesin motors. *Nat Rev Mol Cell Biol* 2009;10:765–77.
- [23] Nitta R, Kikkawa M, Okada Y, Hirokawa N. KIF1A alternately uses two loops to bind microtubules. *Science* 2004;305:678–83.
- [24] Kikkawa M, Hirokawa N. High-resolution cryo-EM maps show the nucleotide binding pocket of KIF1A in open and closed conformations. *EMBO J* 2006;25:4187–94.
- [25] Nitta R, Okada Y, Hirokawa N. Structural model for strain-dependent microtubule activation of Mg-ADP release from kinesin. *Nat Struct Mol Biol* 2008;15:1067–75.
- [26] Krukau A, Knecht V, Lipowsky R. Allosteric control of kinesin's motor domain by tubulin: a molecular dynamics study. *Phys Chem Chem Phys* 2014;16:6189–98.
- [27] Coureux PD, Wells AL, Menetrey J, Yengo CM, Morris CA, Sweeney HL, et al. A structural state of the myosin V motor without bound nucleotide. *Nature* 2003;425:419–23.
- [28] Reubold TF, Eschenburg S, Becker A, Kull FJ, Manstein DJ. A structural model for actin-induced nucleotide release in myosin. *Nat Struct Biol* 2003;10:826–30.
- [29] Adio S, Bloemink M, Hartel M, Leier S, Geeves MA, Woehlke G. Kinetic and mechanistic basis of the nonprocessive Kinesin-3 motor Nckin3. *J Biol Chem* 2006;281:37782–93.
- [30] Sindelar CV, Budny MJ, Rice S, Naber N, Fletterick R, Cooke R. Two conformations in the human kinesin power stroke defined by X-ray crystallography and EPR spectroscopy. *Nat Struct Biol* 2002;9:844–8.
- [31] Rice S, Cui Y, Sindelar C, Naber N, Matuska M, Vale R, et al. Thermodynamic properties of the kinesin neck-region docking to the catalytic core. *Biophys J* 2003;84:1844–54.
- [32] Li J, Jiang J, Qian Q, Xu Y, Zhang C, Xiao J, et al. Mutation of rice BC12/GDD1, which encodes a kinesin-like protein that binds to a GA biosynthesis gene promoter, leads to dwarfism with impaired cell elongation. *Plant Cell* 2011;23:628–40.
- [33] Kull FJ, Endow SA. Force generation by kinesin and myosin cytoskeletal motor proteins. *J Cell Sci* 2013;126:9–19.
- [34] Hackney DD. Highly processive microtubule-stimulated ATP hydrolysis by dimeric kinesin head domains. *Nature* 1995;377:448–50.
- [35] Woehlke G, Ruby AK, Hart CL, Ly B, Hom-Booher N, Vale RD. Microtubule interaction site of the kinesin motor. *Cell* 1997;90:207–16.
- [36] Cochran JC, Gilbert SP. ATPase mechanism of Eg5 in the absence of microtubules: insight into microtubule activation and allosteric inhibition by monastrol. *Biochemistry* 2005;44:16633–48.
- [37] Coy DL, Wagenbach M, Howard J. Kinesin takes one 8-nm step for each ATP that it hydrolyzes. *J Biol Chem* 1999;274:3667–71.
- [38] Kwok BH, Yang JG, Kapoor TM. The rate of bipolar spindle assembly depends on the microtubule-gliding velocity of the mitotic kinesin Eg5. *Curr Biol* 2004;14:1783–8.
- [39] Maliga Z, Kapoor TM, Mitchison TJ. Evidence that monastrol is an allosteric inhibitor of the mitotic kinesin Eg5. *Chem Biol* 2002;9:989–96.
- [40] Rosenfeld SS, Xing J, Jefferson GM, King PH. Docking and rolling, a model of how the mitotic motor Eg5 works. *J Biol Chem* 2005;280:35684–95.
- [41] Wagner MC, Pfister KK, Bloom GS, Brady ST. Copurification of kinesin polypeptides with microtubule-stimulated Mg-ATPase activity and kinetic analysis of enzymatic properties. *Cell Motil Cytoskeleton* 1989;12:195–215.
- [42] Kull FJ, Sablin EP, Lau R, Fletterick RJ, Vale RD. Crystal structure of the kinesin motor domain reveals a structural similarity to myosin. *Nature* 1996;380:550–5.
- [43] Crevel IMTC, Lockhart A, Cross RA. Weak and strong states of kinesin and NCD. *J Mol Biol* 1996;257:66–76.
- [44] Hancock WO, Howard J. Kinesin's processivity results from mechanical and chemical coordination between the ATP hydrolysis cycles of the two motor domains. *Proc Natl Acad Sci USA* 1999;96:13147–52.
- [45] Friel C, Howard J. Coupling of kinesin ATP turnover to translocation and microtubule regulation: one engine, many machines. *J Muscle Res Cell Motil* 2012;33:377–83.
- [46] Oldham ML, Khare D, Quoico FA, Davidson AL, Chen J. Crystal structure of a catalytic intermediate of the maltose transporter. *Nature* 2007;450:515–21.
- [47] Gulick AM, Song H, Endow SA, Rayment I. X-ray crystal structure of the yeast Kar3 motor domain complexed with Mg-ADP to 2.3 Å resolution. *Biochemistry* 1998;37:1769–76.

- [48] Krissinel E, Henrick K. Secondary-structure matching (SSM), a new tool for fast protein structure alignment in three dimensions. *Acta Crystallogr Sect D Biol Crystallogr* 2004;60:2256–68.
- [49] Turner J, Anderson R, Guo J, Beraud C, Fletterick R, Sakowicz R. Crystal structure of the mitotic spindle kinesin Eg5 reveals a novel conformation of the neck-linker. *J Biol Chem* 2001;276:25496–502.
- [50] Song YH, Marx A, Muller J, Woehlke G, Schliwa M, Krebs A, et al. Structure of a fast kinesin: implications for ATPase mechanism and interactions with microtubules. *EMBO J* 2001;20:6213–25.
- [51] Yang Y, Gourinath S, Kovacs M, Nyitray L, Reutzel R, Himmel DM, et al. Rigor-like structures from muscle myosins reveal key mechanical elements in the transduction pathways of this allosteric motor. *Structure* 2007;15:553–64.
- [52] Preller M, Holmes KC. The myosin start-of-power stroke state and how actin binding drives the power stroke. *Cytoskeleton (Hoboken)* 2013;70:651–60.
- [53] Kikkawa M, Sablin EP, Okada Y, Yajima H, Fletterick RJ, Hirokawa N. Switch-based mechanism of kinesin motors. *Nature* 2001;411:439–45.
- [54] Parke CL, Wojcik EJ, Kim S, Worthylake DK. ATP hydrolysis in Eg5 kinesin involves a catalytic two-water mechanism. *J Biol Chem* 2010;285:5859–67.
- [55] Vale RD, Milligan RA. The way things move: looking under the hood of molecular motor proteins. *Science* 2000;288:88–95.
- [56] Sindelar CV, Downing KH. The beginning of kinesin's force-generating cycle visualized at 9-Å resolution. *J Cell Biol* 2007;177:377–85.
- [57] Hirose K, Akimaru E, Toshihiko A, Endow SA, Amos LA. Large conformational changes in a kinesin motor catalyzed by interaction with microtubules. *Mol Cell* 2006;23:913–23.
- [58] Ogawa T, Nitta R, Okada Y, Hirokawa N. A common mechanism for microtubule destabilizers-M type kinesins stabilize curling of the protofilament using the class-specific neck and loops. *Cell* 2004;116:591–602.
- [59] Sindelar CV. A seesaw model for intermolecular gating in the kinesin motor protein. *Biophys Rev* 2011;3:85–100.
- [60] Goulet A, Behnke-Parks WM, Sindelar CV, Major J, Rosenfeld SS, Moores CA. The structural basis of force generation by the mitotic motor kinesin-5. *J Biol Chem* 2012;287:44654–66.
- [61] Gigant B, Wang W, Dreier B, Jiang Q, Pecqueur L, Pluckthun A, et al. Structure of a kinesin-tubulin complex and implications for kinesin motility. *Nat Struct Mol Biol* 2013;20:1001–7.
- [62] Marx A, Hoenger A, Mandelkow E. Structures of kinesin motor proteins. *Cell Motil Cytoskeleton* 2009;66:958–66.
- [63] Sindelar CV, Downing KH. The beginning of kinesin's force-generating cycle visualized at 9-Å resolution. *J Cell Biol* 2007;177:377–85.
- [64] Sindelar CV, Downing KH. An atomic-level mechanism for activation of the kinesin molecular motors. *Proc Natl Acad Sci USA* 2010;107:4111–6.
- [65] Hua W, Young EC, Fleming ML, Gelles J. Coupling of kinesin steps to ATP hydrolysis. *Nature* 1997;388:390–3.
- [66] Karatzaferi C, Chinn MK, Cooke R. The force exerted by a muscle cross-bridge depends directly on the strength of the actomyosin bond. *Biophys J* 2004;87:2532–44.
- [67] Cochran JC, Kull FJ. A molecular motor finds its track. *Nat Struct Mol Biol* 2013;20:920–1.
- [68] Takacs B, O'Neill-Hennessey E, Hetenyi C, Kardos J, Szent-Gyorgyi AG, Kovacs M. Myosin cleft closure determines the energetics of the actomyosin interaction. *FASEB J* 2011;25:111–21.
- [69] Hoyt MA, He L, Loo KK, Saunders WS. Two *Saccharomyces cerevisiae* kinesin-related gene products required for mitotic spindle assembly. *J Cell Biol* 1992;118:109–20.
- [70] Sawin KE, LeGuellec K, Philippe M, Mitchison TJ. Mitotic spindle organization by a plus-end-directed microtubule motor. *Nature* 1992;359:540–3.
- [71] Heck MM, Pereira A, Pesavento P, Yannoni Y, Spradling AC, Goldstein LS. The kinesin-like protein KLP61F is essential for mitosis in *Drosophila*. *J Cell Biol* 1993;123:665–79.
- [72] Blangy A, Lane HA, d'Herin P, Harper M, Kress M, Nigg EA. Phosphorylation by p34cdc2 regulates spindle association of human Eg5, a kinesin-related motor essential for bipolar spindle formation *in vivo*. *Cell* 1995;83:1159–69.
- [73] McIntosh JR, Hepler PK, Van Wie DG. Model for mitosis. *Nature* 1969;224:659–63.
- [74] Saxton WM, McIntosh JR. Interzone microtubule behavior in late anaphase and telophase spindles. *J Cell Biol* 1987;105:875–86.
- [75] Ke A, Wolberger C. Insights into binding cooperativity of MATa1/MATalpha2 from the crystal structure of a MATa1 homeodomain-maltose binding protein chimera. *Protein Sci* 2003;12:306–12.
- [76] Duan D, Hnatchuk DJ, Brenner J, Davis D, Allingham JS. Crystal structure of the Kar3-like kinesin motor domain from the filamentous fungus *Ashbya gossypii*. *Proteins* 2012;80:1016–27.
- [77] Talje L, Ben El Kadhi K, Atchia K, Tremblay-Boudreault T, Carreno S, Kwok BH. DHTP is an allosteric inhibitor of the kinesin-13 family of microtubule depolymerases. *FEBS Lett* 2014;588(14):2315–20.
- [78] Hyman A, Drechsel D, Kellogg D, Salser S, Sawin K, Steffen P, et al. Preparation of modified tubulins. *Methods Enzymol* 1991;196:478–85.
- [79] Otwinowski Z, Minor W. Processing of X-ray diffraction data collected in oscillation mode. *Methods Enzymol* 1997;276:307–26.
- [80] Long F, V.A.A., Young P, Murchudov GN. *BALBES*: a molecular-replacement pipeline. *Acta Crystallogr Sect D Biol Crystallogr* 2008;64:125–32.
- [81] McCoy A, J.G.-K., R.W., Storoni LC, Read RJ. Likelihood-enhanced fast translation functions. *Acta Crystallogr Sect D Biol Crystallogr* 2005;61:458–64.
- [82] Emsley P, Cowtan K. Coot: model-building tools for molecular graphics. *Acta Crystallogr Sect D Biol Crystallogr* 2004;60:2126–32.
- [83] Murshudov GN, Skubak P, Lebedev AA, Pannu NS, Steiner RA, Nicholls RA, et al. REFMAC5 for the refinement of macromolecular crystal structures. *Acta Crystallogr Sect D Biol Crystallogr* 2011;67:355–67.
- [84] Solinet S, Mahmud K, Stewman SF, Ben El Kadhi K, Decelle B, Talje L, et al. The actin-binding ERM protein Moesin binds to and stabilizes microtubules at the cell cortex. *J Cell Biol* 2013;202:251–60.
- [85] Kapoor TM, Mitchison TJ. Allele-specific activators and inhibitors for kinesin. *Proc Natl Acad Sci USA* 1999;96:9106–11.
- [86] Sosa H, Dias DP, Hoenger A, Whittaker M, Wilson-Kubalek E, Sablin E, et al. A model for the microtubule-NCD motor protein complex obtained by cryo-electron microscopy and image analysis. *Cell* 1997;90:217–24.
- [87] Tan D, Rice WJ, Sosa H. Structure of the kinesin13-microtubule ring complex. *Structure* 2008;16:1732–9.
- [88] Asenjo Ana B, Chatterjee C, Tan D, DePaoli V, Rice William J, Diaz-Avalos R, et al. Structural model for tubulin

- recognition and deformation by kinesin-13 microtubule depolymerases. *Cell Rep* 2013;3:759–68.
- [89] Henderson R, Sali A, Baker ML, Carragher B, Devkota B, Downing Kenneth H, et al. Outcome of the first electron microscopy validation task force meeting. *Structure* 2012;20:205–14.
- [90] Rosenthal PB, Henderson R. Optimal determination of particle orientation, absolute hand, and contrast loss in single-particle electron cryomicroscopy. *J Mol Biol* 2003;333:721–45.
- [91] Pettersen EF, Goddard TD, Huang CC, Couch GS, Greenblatt DM, Meng EC, et al. UCSF Chimera—a visualization system for exploratory research and analysis. *J Comput Chem* 2004;25:1605–12.
- [92] Gouet P, Robert X, Courcelle E. ESPript/ENDscript: extracting and rendering sequence and 3D information from atomic structures of proteins. *Nucleic Acids Res* 2003;31:3320–3.
- [93] DeLano WL. (2002). The PyMOL Molecular Graphics System, Version 1.5.0.4 Schrödinger, LLC.